Accepted Manuscript

On the thermal buckling analysis of functionally graded plates with internal defects using extended isogeometric analysis

Tiantang Yu, Tinh Quoc Bui, Shuohui Yin, Duc Hong Doan, C.T. Wu, Thom Van Do, Satoyuki Tanaka

On the thermal buckling analysis of functionally graded plates with internal defects using extended isogeometric analysis

Tiantang Yu [a,*], Tinh Quoc Bui[b,*], Shuohui Yin[a], Duc Hong Doan[c], C.T. Wu[d],
Thom Van Do[e], Satoyuki Tanaka[f]

[a] *Department of Engineering Mechanics, Hohai University, Nanjing 210098, PR China.*

[b] *Department of Mechanical and Environmental Informatics, Tokyo Institute of Technology,*
2-12-1-W8-22, Ookayama, Meguro-ku, Tokyo 152-8552, Japan.

[c] *Department of Mechanical and Control Engineering, Tokyo Institute of Technology,*
Japan

[d] *Livermore Software Technology Corporation, Livermore, CA 94550, USA*

[e] *Department of Mechanics, Le Quy Don Technical University, 236 Hoang Quoc Viet,*
Hanoi, Vietnam

[f] *Graduate School of Engineering, Hiroshima University, Japan*

Highlight

- New results of critical thermal buckling temperature rise of FGPs with internal defects are presented.

- An effective and accurate thermal buckling XIGA/level sets using FSDT for FGPs with internal defects is developed.

- New approach eliminates the need for trimmed NURBS surface to describe cutouts.

- The defects have a significant impact on the critical thermal buckling temperature.

[*]Corresponding authors. Tel.: +86 (25) 52430342(T.T. Yu), +81 (70) 21506399 (T.Q. Bui)

E-mail addresses: tiantangyu@hhu.edu.cn (T.T. Yu), tinh.buiquoc@gmail.com (T.Q. Bui)

Abstract

We investigate new numerical results of thermal buckling for functionally graded plates (FGPs) with internal defects (e.g., crack or cutout) using an effective numerical method. The new formulation employs the first-order shear deformation plate theory associated with extended isogeometric analysis (XIGA) and level sets. The material properties of FGPs are assumed to vary continuously through the plate thickness obeying a power function. The internal defects are represented by the level sets, while the shear-locking effect is eliminated by a special treatment, multiplying the shear terms by a factor. In XIGA, the isogeometric approximation enhanced by enrichment is cable of capturing discontinuities in plates caused by internal defects. The internal discontinuity is hence independent of the mesh, and the trimmed NURBS surface to describe the geometrical structure with cutouts is no longer required. Five numerical examples are considered and numerical results of the critical buckling temperature rise (CBTR) of FGPs computed by the proposed method are analyzed and discussed. The accuracy of the method is demonstrated by validating the obtained numerical results against reference solutions available in literature. The influences of various aspect ratios including gradient index, crack length, plate thickness, cutout size, and boundary conditions on the CBTR are investigated.

1. Introduction

Although the functionally graded materials (FGMs) in general or the functionally graded plates (FGPs) in particular have been extensively used in many engineering applications [1], however, the FGPs may develop defects or flaws during manufacturing or in-service suffering external loading conditions. In addition to the defects, the inner cutouts with different shapes are often created in the plate elements as many practical requirements. The presence of defects/flaws or such inner cutouts greatly affects the mechanical behaviors of structures and their performance in whole or part. Consequently it is very important to understand the mechanical response of FGPs with internal flaws [2,3]. The temperature rising in plates produces in-plane compressible forces which make the

2

structures to be buckled before reaching to a yield stress, and the structure suffers large deformation behavior and reduces load carrying capacity at the buckling state. Consequently, the thermal buckling problem under study plates plays an important role in practical application. This paper thus focuses particularly on the study of thermal buckling phenomena of FGPs with internal flaws under the variation of the temperature.

It is fairly well covered in the literature on the investigation of thermal buckling behavior of FGPs. Javaheri and Eslami [4] presented closed-form solutions for thermal buckling of FGPs under four types of thermal loads. Shariat and Eslami [5] developed closed-form solutions for mechanical and thermal buckling of thick FGPs using the third order shear deformation theory (TSDT). Woo and Meguid [6] analytically investigated the thermo-mechanical post-buckling of FGPs and shallow cylindrical shells. Also in closed-form, Najafizadeh and Heydari [7] analyzed the critical thermal buckling temperature of functionally graded circular plates using the TSDT. Khalfi et al. [8] proposed a refined shear deformation theory and applied it to analyze thermal buckling of solar FGPs with simply supported boundary conditions and resting on elastic foundation. Malekzadeh [9] studied thermal buckling of functionally graded arbitrary straight-sided quadrilateral plates based on 3D elasticity theory, and the Trefftz criterion was used to obtain the stability equations. The effect of geometrical imperfections on thermal buckling of FGPs was investigated by Shariat and Eslami [10]. Jaberzadeh et al. [11] used the element-free Galerkin method for thermal buckling analysis of functionally graded skew and trapezoidal plates, while Zhao et al. [12] explored the mechanical and thermal buckling behaviors of FGPs using the first-order shear deformation plate theory (FSDT) in conjunction with the element-free kp-Ritz method.

Nevertheless, studies on thermal buckling failure behaviors of FGPs with internal defects are rather rare. Thermal buckling of FGPs with temperature dependent material properties and containing a central circular cutout was investigated by Saji et al. [13]. Thermal buckling of composite plates with a circular cutout was investigated by Shaterzadeh et al. [14] using the finite element method (FEM), and the effect of boundary conditions, cutout size and plate aspect ratio on critical thermal buckling temperature was explored. Recently, Natarajan et al. [15] examined the effect of local defects such as cracks

and cutouts on the buckling behaviour of FGPs subjected to mechanical and thermal load using the extended finite element method (XFEM) and the FSDT.

Isogeometric analysis (IGA) [16] is a new numerical method that shares the same splines basis function in representing the geometry in design and solution approximations in analysis. The IGA is based on CAD splines (e.g., NURBS), and proved to be an efficient, highly accurate, robust and higher order continuity approach. The desirable characteristics of IGA make it superior to the traditional FEM in some aspects as it has successfully applied to many engineering problems, e.g., see [17-24].

Similar to the XFEM, the standard IGA approximation is enriched with some special functions around the discontinuities in the framework of partition of unity to create a novel method, namely, the so-called extended isogeometric analysis (XIGA) [20, 25]. The XIGA contains the inherent advantages of both IGA and local enriched partition-of-unity method (XFEM). The XIGA has been applied to solve linear elastic fracture mechanics problems [25-28], static and dynamic cracks in piezoelectric materials [20], curved interface problems [29], vibration analysis of cracked FGM plates [30], and stochastic fatigue crack growth of interfacial crack in bi-layered FGMs [31].

In this paper, we investigate the thermal buckling behaviors of FGPs with internal defects such as cracks or cutouts using NURBS–based XIGA with level sets and the FSDT. Parametric studies are performed by investigating the critical temperature value versus various aspect ratios including the gradient index, crack location, crack length, width-to-thickness, boundary conditions, and cutout size. The nature of the tensor product of the NURBS basis functions induces the difficulty in treating the trimmed objects like internal cutouts, as a result of very complicated tasks in modeling cutouts using the conventional NURBS-based IGA. In the contrary, by using the level sets in describing the discontinuities and the discontinuities are independent of the mesh, so the trimmed NURBS surface to describe the geometrical structure with cutouts is thus no longer required.

The body of the paper is outlined as follows. Problem model of FGPs is described in Section 2. In Section 3, XIGA formulation for thermal buckling analysis of plates with internal defects is derived. Numerical results and discussions are provided in Section 4.

4

Section 5 closes with some concluding remarks.

2. Problem model definition

2.1. Functional graded materials

In this work, a ceramic-metal FGP with thickness h is considered. The bottom and top faces of the plate are assumed to be fully metal and ceramic, respectively, and the gradient properties changed along with z-direction as depicted in Fig. 1. The xy-plane reveals the mid-plane of the plate, while the positive z-axis is upward from the mid-plane. The Poisson's ratio v is assumed to be constant throughout the study, but the Young's modulus E and thermal expansion coefficeint α vary through the thickness with a power law distribution:

$$E(z) = E_m + (E_c - E_m)\left(\frac{1}{2} + \frac{z}{h}\right)^n \tag{1}$$

$$\alpha(z) = \alpha_m + (\alpha_c - \alpha_m)\left(\frac{1}{2} + \frac{z}{h}\right)^n \tag{2}$$

where n denotes the gradient index, z is the thickness coordinate variable with $-h/2 \le z \le h/2$, and subscripts c and m represent the ceramic and metal constituents, respectively.
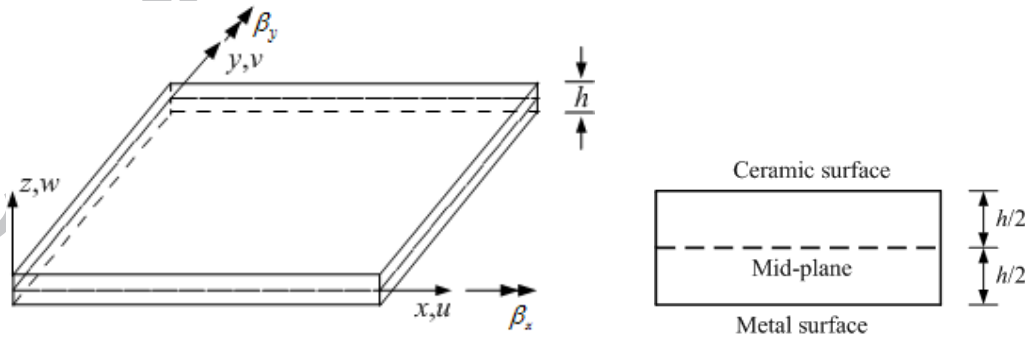

Fig .1 Schematic geometry of an FGP.

2.2. Kinematic equations of plates

Based on the first order shear deformation plate theory (FSDT), the displacements u, v,

w at a point (x, y, z) in the plate, see Fig. 1, are expressed as

$$u(x, y, z) = u_0(x, y) + z\beta_x(x, y) \tag{3a}$$

$$v(x, y, z) = v_0(x, y) + z\beta_y(x, y) \tag{3b}$$

$$w(x, y, z) = w_0(x, y) \tag{3c}$$

where u_0, v_0, w_0 are the mid-plane displacements components in the x, y, z axes, respectively. β_x and β_y are the transverse normal rotations in the xz- and yz- planes of mid-plane.

By making the usual small strain assumptions, the strains are expressed in the following matrix form

$$\boldsymbol{\varepsilon} = \left\{ \begin{array}{c} \boldsymbol{\varepsilon}_p \\ \mathbf{0} \end{array} \right\} + \left\{ \begin{array}{c} z\boldsymbol{\varepsilon}_b \\ \boldsymbol{\gamma}_s \end{array} \right\} \tag{4}$$

with

$$\boldsymbol{\varepsilon}_p = \left\{ \begin{array}{c} u_{0,x} \\ v_{0,y} \\ u_{0,y} + v_{0,x} \end{array} \right\}, \quad \boldsymbol{\varepsilon}_b = \left\{ \begin{array}{c} \beta_{x,x} \\ \beta_{y,y} \\ \beta_{x,y} + \beta_{y,x} \end{array} \right\}, \quad \boldsymbol{\gamma}_s = \left\{ \begin{array}{c} \beta_x + w_{0,x} \\ \beta_y + w_{0,y} \end{array} \right\} \tag{5}$$

According to Hooke's law for plane stress elastic problem, the stresses can be written as

$$\boldsymbol{\sigma} = \mathbf{D}_m(z)\left(\boldsymbol{\varepsilon}_p + z\boldsymbol{\varepsilon}_b - \boldsymbol{\varepsilon}_T\right) \ , \quad \boldsymbol{\tau} = \mathbf{D}_s(z)\boldsymbol{\gamma} \tag{6}$$

with

$$\boldsymbol{\sigma} = \begin{bmatrix} \sigma_x & \sigma_y & \tau_{xy} \end{bmatrix}^T \tag{7a}$$

$$\mathbf{D}_m(z) = \frac{E(z)}{1-v^2} \begin{bmatrix} 1 & v & 0 \\ v & 1 & 0 \\ 0 & 0 & (1-v)/2 \end{bmatrix} \tag{7b}$$

$$\boldsymbol{\varepsilon}_T = \alpha(z)\Delta T \begin{bmatrix} 1 & 1 & 0 \end{bmatrix}^T \tag{7c}$$

$$\boldsymbol{\tau} = \begin{bmatrix} \tau_{xz} & \tau_{yz} \end{bmatrix}^T \tag{7d}$$

$$\mathbf{D}_s(z) = \frac{kE(z)}{2(1+v)} \begin{bmatrix} 1 & 0 \\ 0 & 1 \end{bmatrix} \tag{7e}$$

6

$$\boldsymbol{\gamma} = \begin{bmatrix} \gamma_{xz} & \gamma_{yz} \end{bmatrix}^T \tag{7f}$$

where $\alpha(z)$ is the coefficient of thermal expansion, ΔT is the temperature change, k is the shear correction factor, and $k = 5/6$ is adopted in this study.

2.3 Weak-form

For the buckling analysis, the weak-form can be expressed as follows:

$$\int_\Omega \delta\boldsymbol{\varepsilon}^T \mathbf{D}\boldsymbol{\varepsilon}\, d\Omega + \int_\Omega \delta\boldsymbol{\gamma}^T \mathbf{D}^s \boldsymbol{\gamma}\, d\Omega - \int_\Omega \delta\boldsymbol{\varepsilon}^T \overline{\mathbf{D}}\boldsymbol{\varepsilon}_T\, d\Omega + \int_\Omega \nabla^T \delta w \mathbf{N}_0 \nabla w\, d\Omega = 0 \tag{8}$$

where

$$\boldsymbol{\varepsilon} = \begin{bmatrix} \boldsymbol{\varepsilon}_p \\ \boldsymbol{\varepsilon}_b \end{bmatrix} \tag{9a}$$

$$\mathbf{D} = \begin{bmatrix} \mathbf{D}^m & \overline{\mathbf{B}} \\ \overline{\mathbf{B}} & \mathbf{D}^b \end{bmatrix} \tag{9b}$$

$$\mathbf{D}^m = \int_{-h/2}^{h/2} \mathbf{D}_m(z)\, dz \tag{9c}$$

$$\overline{\mathbf{B}} = \int_{-h/2}^{h/2} z\mathbf{D}_m(z)\, dz \tag{9d}$$

$$\mathbf{D}^b = \int_{-h/2}^{h/2} z^2 \mathbf{D}_m(z)\, dz \tag{9e}$$

$$\mathbf{D}^s = \int_{-h/2}^{h/2} \mathbf{D}_s(z)\, dz \tag{9f}$$

$$\overline{\mathbf{D}} = \begin{bmatrix} \mathbf{D}^m \\ \overline{\mathbf{B}} \end{bmatrix} \tag{9g}$$

and $\nabla^T = \begin{bmatrix} \partial/\partial x & \partial/\partial y \end{bmatrix}^T$ is the gradient operator, $\mathbf{N}_0 = \begin{bmatrix} N_x^0 & N_{xy}^0 \\ N_{xy}^0 & N_y^0 \end{bmatrix}$ is the in-plane resultant forces under temperature change.

3. XIGA formulation for thermal buckling of plates with internal defects

3.1 The NURBS basis functions

A knot vector in one dimension is a set of non-decreasing numbers in the parametric space, that is $k(\xi) = \{\xi_1, \xi_2, ..., \xi_{n+p+1}\}$, $\xi_i \le \xi_{i+1}$, where $\xi_i \in [0,1]$, and ξ_i is the ith knot, n and p are the number of basis functions and the order of the B-spline basis function,

respectively. Given a knot vector $k(\xi)$, the B-spline basis function $N_{i,p}(\xi)$ is defined recursively as follows [20, 32]:

$$N_{i,0}(\xi) = \begin{cases} 1 & \xi_i \leq \xi < \xi_{i+1} \\ 0 & \text{otherwise} \end{cases} \tag{10}$$

and

$$N_{i,p}(\xi) = \frac{\xi - \xi_i}{\xi_{i+p} - \xi_i} N_{i,p-1}(\xi) + \frac{\xi_{i+p+1} - \xi}{\xi_{i+p+1} - \xi_{i+1}} N_{i+1,p-1}(\xi) \quad \text{for} \quad p \geq 1 \tag{11}$$

For two-dimensional problem, the NURBS basis functions can be constructed by taking the tensor product of two one-dimensional B-spline basis functions as [20, 32]

$$R_{i,j}^{p,q}(\xi,\eta) = \frac{N_{i,p}(\xi)N_{j,q}(\eta)w_{i,j}}{\sum\limits_{i=1}^{n}\sum\limits_{j=1}^{m}N_{i,p}(\xi)N_{j,q}(\eta)w_{i,j}} \tag{12}$$

where $N_{i,p}(\xi)$ and $N_{j,q}(\eta)$ are the B-spline basis functions of order p in the ξ direction and order q in the η direction, respectively; $N_{j,q}(\eta)$ follows the recursive formula shown in Eqs. (10) and (11) with knot vector $k(\eta)$, and the definition of $k(\eta)$ is similar to that of $k(\xi)$; $w_{i,j}$ represents the weight.

3.2. The XIGA

Compared with the conventional XFEM, the XIGA utilizes the NURBS basis functions instead of the Lagrange polynomials in the approximation of the displacement field. Owing to the higher-order continuity of NURBS, the obtained stresses are smooth which is unavailable in XFEM with C^0-continuity of inter-element.

3.2.1 XIGA approximations for plate with cracks

The deflection and rotations of plates using the XIGA can be approximated as follows [33-36]:

$$\begin{aligned}
\left(u_i^h, v_i^h, w_i^h\right)(\boldsymbol{x}) &= \sum_{i \in \boldsymbol{N}^s} R_i(\boldsymbol{x})(u_i, v_i, w_i) + \sum_{j \in \boldsymbol{N}^{cut}} R_j(\boldsymbol{x})\left(H(\boldsymbol{x}) - H(\boldsymbol{x}_j)\right)\left(b_j^u, b_j^v, b_j^w\right) \\
&+ \sum_{k \in \boldsymbol{N}^{tip}} R_k(\boldsymbol{x})\left(\sum_{l=1}^{4}\left(c_{kl}^u, c_{kl}^v, c_{kl}^w\right)\left(\boldsymbol{G}_l(r,\theta) - \boldsymbol{G}_l(r_k,\theta_k)\right)\right)
\end{aligned} \tag{13a}$$

$$\left(\beta_x^h,\beta_y^h\right)(x)=\sum_{i\in N^s}R_i(x)\left(\beta_{xi},\beta_{yi}\right)+\sum_{j\in N^{cut}}R_j(x)\left(H(x)-H\left(x_j\right)\right)\left(b_j^{\beta_x},b_j^{\beta_y}\right)+$$

$$+\sum_{k\in N^{tip}}R_k(x)\left(\sum_{l=1}^{4}\left(c_{kl}^{\beta_x},c_{kl}^{\beta_y}\right)\left(F_l(r,\theta)-F_l(r_k,\theta_k)\right)\right)$$
(13b)

where $R_i(x)$, $R_j(x)$, and $R_k(x)$ are the NURBS basis functions; N^s is the set of all control points in the discretization; N^{cut} is the set of control points whose basis function support is entirely split by the crack, and are enriched with a modified Heaviside step function $H(x)$ which takes on the value +1 above the crack and -1 below the crack; N^{tip} is the set of control points whose basis function support is partly split by the crack, and are enriched with the crack-tip branch enrichment functions; u_i, v_i, w_i, β_x and β_y represent the unknown vectors associated with the continuous part of the finite element solution, respectively, b_j is the additional enriched degree of freedom vector at the node associated with the modified Heaviside function, and c_{kl} denotes the additional enriched degree of freedom vector associated with the elastic asymptotic crack-tip functions. The asymptotic crack-tip functions are given by [33-36]

$$\mathbf{G}_l(r,\theta)=\left\{r^{\frac{3}{2}}\sin\left(\frac{\theta}{2}\right),r^{\frac{3}{2}}\cos\left(\frac{\theta}{2}\right),r^{\frac{3}{2}}\sin\left(\frac{3\theta}{2}\right),r^{\frac{3}{2}}\cos\left(\frac{3\theta}{2}\right)\right\}$$
(14a)

$$\mathbf{F}_l(r,\theta)=\left\{r^{\frac{1}{2}}\sin\left(\frac{\theta}{2}\right),r^{\frac{1}{2}}\cos\left(\frac{\theta}{2}\right),r^{\frac{1}{2}}\sin\left(\frac{\theta}{2}\right)\sin(\theta),r^{\frac{1}{2}}\cos\left(\frac{\theta}{2}\right)\sin(\theta)\right\}$$
(14b)

3.2.2 XIGA approximation for plate with cutouts

According to [37], the deflection and rotations of plate with cutouts using the XIGA can be approximated as

$$\left(u_i^h,v_i^h,w_i^h\right)(x)=\sum_{i\in N^s}\overline{H}(x)R_i(x)(u_i,v_i,w_i)$$
(15a)

$$\left(\beta_x^h,\beta_y^h\right)(x)=\sum_{i\in N^s}\overline{H}(x)R_i(x)\left(\beta_{xi},\beta_{yi}\right)$$
(15b)

with

$$\overline{H}(x)=\begin{cases}1 & x\in\Omega\\0 & x\notin\Omega\end{cases}$$
(16)

9

Remark #1: In practice, we may implement the displacement functions similar to that in the conventional IGA, instead of the displacement function described in Eq. (15), and merely remove the integral on the cutout part in the calculation of the stiffness matrix, and the geometrical stiffness matrix.

Remark #2: In the XIGA, it should be stressed out here that the boundary of the cutout is represented by the zero level curves. The boundary is located from the value of the level set information stored at the nodes, thus the trimmed NURBS surface is no longer required to describe the geometrical structure with cutouts [38].

3.3 Discrete equations

Substituting Eq. (13) into Eq. (5), the in-plane, bending and shear strains can be rewritten as

$$\left[\boldsymbol{\varepsilon}_p^T \quad \boldsymbol{\varepsilon}_b^T \quad \boldsymbol{\gamma}^T \right]^T = \sum_{i=1}^{m \times n} \left[\left(\mathbf{B}_i^p \right)^T \quad \left(\mathbf{B}_i^b \right)^T \quad \left(\mathbf{B}_i^s \right)^T \right]^T \boldsymbol{\delta}_i \tag{17}$$

where $\boldsymbol{\delta}_i$ is the vector of nodal degrees of freedom associated with the control point i, including the continuous displacements and enriched variables, and

$$\mathbf{B} = \left[\mathbf{B}^{std} \, \middle| \, \mathbf{B}^{enr} \right] \tag{18}$$

where $\mathbf{B}^{std}$ and $\mathbf{B}^{enr}$ are the standard and enriched strain matrices of $\mathbf{B}$ defined in the following forms

$$\mathbf{B}_i^p = \begin{bmatrix} \bar{N}_{i,x} & 0 & 0 & 0 & 0 \\ 0 & \bar{N}_{i,y} & 0 & 0 & 0 \\ \bar{N}_{i,y} & \bar{N}_{i,x} & 0 & 0 & 0 \end{bmatrix} \tag{19a}$$

$$\mathbf{B}_i^b = \begin{bmatrix} 0 & 0 & 0 & \bar{N}_{i,x} & 0 \\ 0 & 0 & 0 & 0 & \bar{N}_{i,y} \\ 0 & 0 & 0 & \bar{N}_{i,y} & \bar{N}_{i,x} \end{bmatrix} \tag{19b}$$

$$\mathbf{B}_i^s = \begin{bmatrix} 0 & 0 & \bar{N}_{i,x} & 0 & 0 \\ 0 & 0 & \bar{N}_{i,y} & 0 & 0 \end{bmatrix} \tag{19c}$$

where $\bar{N}_i$ can be either the NURBS basis functions $R_i(x)$ or enriched functions

$$R_j(x)\big(H(x)-H(x_j)\big) \quad , \quad R_k(x)\left(\sum_{l=1}^{4}\big(G_l(r,\theta)-G_l(r_k,\theta_k)\big)\right) \quad ,$$

$$R_k(x)\left(\sum_{l=1}^{4}\big(F_l(r,\theta)-F_l(r_k,\theta_k)\big)\right).$$

Substituting Eq. (13) with relation in Eq. (17) into Eq. (8), the eigenvalue formulations of buckling plate problem can be rewritten as

$$(\mathbf{K}+\lambda_{cr}\mathbf{K}_G)\boldsymbol{\delta}=0 \tag{20}$$

where λ_{cr} is the critical buckling load; and $\mathbf{K}$ and $\mathbf{K}_G$ are the global stiffness matrix and geometrical stiffness matrix, respectively, which are expressed as

$$\mathbf{K}=\int_{\Omega}\left\{\mathbf{B}^p \quad \mathbf{B}^b\right\}\mathbf{D}\left\{\mathbf{B}^p \quad \mathbf{B}^b\right\}^T+\mathbf{B}^{sT}\overline{\mathbf{D}}^s\mathbf{B}^s d\Omega \tag{21}$$

$$\mathbf{K}_G=\int_{\Omega}\mathbf{G}_b^T\mathbf{N}_0\mathbf{G}_b d\Omega \tag{22}$$

with

$$\mathbf{G}_{bi}=\begin{bmatrix} 0 & 0 & \overline{N}_{i,x} & 0 & 0 \\ 0 & 0 & \overline{N}_{i,y} & 0 & 0 \end{bmatrix} \tag{23}$$

3.4 Treatment of shear-locking effect

The shear locking also appears in low-order NURBS isogeometric elements for the very thin plate [19]. The shear locking is suppressed by introducing a modification factor into the shear terms, and the modified material matrix related to shear terms is given as [33]

$$\overline{\mathbf{D}}^s=\mathbf{D}^s\frac{h^2}{h^2+\alpha l^2} \tag{24}$$

where l is the longest length of edges of the NURBS element and $\alpha=0.1$ is selected in this study.

4. Numerical results and discussions

In this section, the thermal buckling analysis of FGPs with through-thickness crack or cutout using the proposed XIGA is presented. In all numerical calculations, the cubic order NURBS basis functions are used. For the numerical integration, a 4×4 Gaussian

11

quadrature scheme is assigned for the normal elements, while a triangular sub-domain technique is applied to the elements which are cut by crack or cutout. All the plates being studied are considered under uniaxial load. The critical buckling temperature rise (CBTR), which is solved directly from the eigenvalue equation of buckling plates by the developed XIGA, is numerically analyzed.

For convenience in representing the numerical results, different boundaries of the plate are named as simply supported (S), clamped (C), and free (F). For the clamped boundary conditions, the rotations are obtained from the derivatives of transverse deflection. The constraint on the rotations is hence imposed by fixing the transverse defection with two rows of control points as described in [19]. Throughout the study, two FGPs made of Al/Al$_2$O$_3$ and Al/ZrO$_2$ material with their material parameters in Table 1 are considered.

Table 1

Properties of the functionally graded material components.

Material	Properties		
	E (GPa)	ν	α (/^{o}C)
Aluminium (Al)	70	0.3	23×10^{-6}
Alumina (Al$_2$O$_3$)	380	0.3	7.4×10^{-6}
Zirconia (ZrO$_2$)	151	0.3	10×10^{-6}

4.1. Convergence and accuracy studies

The thermal buckling of a square Al/Al$_2$O$_3$ plate (*a*=*b*=0.2m) subjected to a uniform temperature rise is considered, verifying the convergence property and the accuracy of the developed XIGA method based on the FSDT. All the boundaries of plate are fully clamped. We typically consider two plate thickness ratios, for instance, *a/h*=50 and 100, and various values of the volume fraction exponent taken from 0 to 5. As reported in Table 2, the CBTR calculated by the present XIGA for the two specified thickness ratios converges well to the reference solutions [12] as the physical mesh gets finer. The reference solutions [12] were derived based on the FSDT in conjunction with the element-free *kp*-Ritz method,

in which the displacement field is approximated by a set of mesh-free kernel particle functions while the bending stiffness is evaluated using a stabilized conforming nodal integration technique. The present numerical results of the CBTR also reveal one interesting issue that even a very coarse mesh (e.g., 8×8) can also yield acceptable solutions, demonstrating one of the advantages of the XIGA as compared with the FEM which often requires fine meshes for the solution. In the rest of the manuscript, we however use a regular physical fine mesh for all the computational models, which is to just ensure the accuracy of the solutions.

Also in Table 2, when the plate becomes more and more metal, i.e., increasing the volume fraction exponent (n), the CBTR initially decreases for n ranging from 0 to 2, and a slight change of the CBTR is observed when escalating n further to 5. The decrease of the CBTR from 0 to 2 is significant, in about twice. This phenomenon can also be found the same for the reference solutions utilizing the element-free kp-Ritz method [12]. The decrease of the CBTR may be due to the fact that the elasticity modulus of the metal (Al) is much smaller than that of the ceramic (Al_2O_3) (see Table 1 for the material parameters), implying that the ceramic is stiffener, and that makes the critical buckling coefficient larger. More interestingly, it can be concluded that the thinner plates (e.g., a/h=100) undergo a smaller CBTR than the thicker ones (e.g., a/h=50). This conclusion can be found from the reference work [12] as well.

Table 2

Comparison of the CBTR of a fully clamped square Al/Al_2O_3 plate for different aspect thickness-to-length ratios altered by the volume fraction exponents obtained by the developed XIGA and the reference solutions [12].

a/h	Elements	The volume fraction exponent (n)				
		0	0.5	1	2	5
100	4×4	52.534	30.186	24.932	22.065	22.251
	8×8	45.468	25.777	21.143	18.742	19.315
	16×16	45.268	25.652	21.035	18.647	19.232
	20×20	45.266	25.651	21.034	18.646	19.231
	24×24	45.265	25.650	21.033	18.646	19.231
	Ref. [12]	44.171	24.899	20.771	18.489	19.150
50	4×4	190.710	108.582	89.245	79.059	80.906
	8×8	180.360	102.266	83.876	74.340	76.585
	16×16	180.132	102.123	83.752	74.232	76.490
	20×20	180.128	102.121	83.751	74.230	76.489
	24×24	180.127	102.120	83.750	74.230	76.488
	Ref. [12]	175.817	99.162	82.357	71.013	74.591

In order to prove the validity of the present procedure, the thermal buckling of a square Al/Al$_2$O$_3$ simply-supported plate (a=b=1m) with thickness to span ratio h/a=0.2 subjected to a uniform temperature rise is further considered. Various values of the volume fraction exponent taken from 0 to 3 are examined. As reported in Fig. 2, the values of CBTR calculated by the present XIGA are in good agreement with the semi-analytical solutions [39].
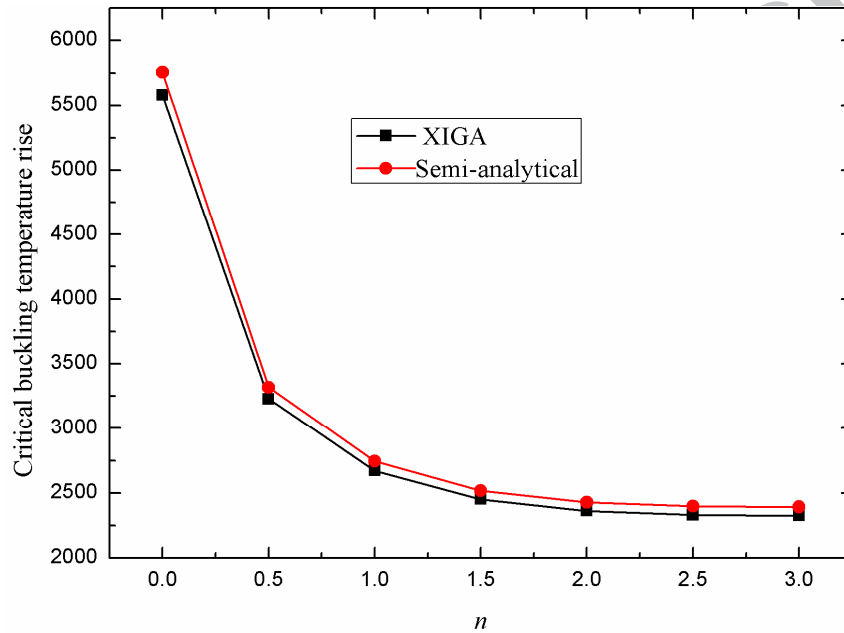

Fig. 2 Critical buckling temperature of FGM plate under uniform temperature rise vs gradient index of the plate.

4.2. An edge cracked rectangular FGP

Next numerical example deals with a rectangular Al/Al$_2$O$_3$ plate with an edge crack as shown in Fig. 3. The length and width of plate are set up to be a =2m, and b = 1m. The crack is assumed to be parallel to the *x*-axis. A regular mesh of 31$\times$15 elements is used for the analysis. Different boundary conditions of plate including CCCC, SCSC, SSSS and SFSF are taken. The CBTR as a function of the volume fraction exponent (n) is calculated by using the proposed method and is then sketched in Fig. 4. The present CBTR results of the Al/Al$_2$O$_3$ plate shown in Fig. 4 are to show the effect of the boundary conditions on the

CBTR coefficient. In addition, both the plates with and without cracks are taken into account, which is to further interpret the influence of the defect or crack on the CBTR. We select a crack length of *c/a*=0.5 for the investigation.

First, it is evident that the effect of the crack on the CBTR of FGPs is significant as the CBTR are found largely different between the plates with and without crack. The CBTR induced by the plates with crack is smaller than that caused by the perfect plates. It means that the imperfect plates get highly critical as compared with the perfect ones. Loosely speaking, the structures suffering defects or cracks are easily to get damaged or destroyed in the critical buckling circumstance. However, a great effect of the crack on the CBTR takes place clearly for the boundary conditions CCCC, SSSS and the SCSC, while nothing really has been seen to the SFSF. Generally, when the plates become more freely in constrain, the CBTR may become similarly. Anyway, the results are very interesting since it shows us one of the reasons why the studies on the cracks under thermal buckling load are important.

Also in Fig. 4, it is again found that the CBTR decreases with increasing the volume fraction exponent. It is indicated clearly a great impact of the volume fraction on the FGMs, especially exhibiting a great difference on the CBTR behaviors among the ceramic and the ones whose properties become more and more metal.

Further observation on the numerical CBTR results in Fig. 4, and additionally presented in Table 3, shows us a strong influence of the boundary conditions on the CBTR. The crack alters the CBTR as it is found to be decreased for the CCCC and SSSS and SCSC boundary conditions. The CBTR of the CCCC is much greater than that of a SSSS as well as other boundary conditions. In view of this, since the thermal expansion coefficient raising from ceramic to metal, approximately three time as seen in Table 1, the thermal body forces or constrains make the CBTR decreases when increasing the volume fraction exponents as well as when varying the boundary conditions.
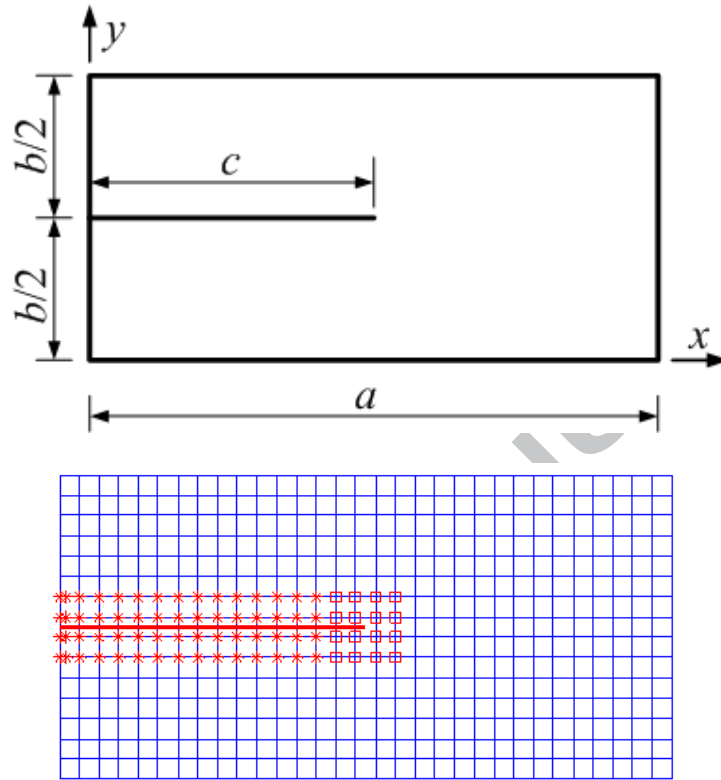
Fig. 3 Model geometry of a rectangular FGP with an edge crack and its regular physical mesh of 31×15 elements. The "*star*" sign represents the enriched elements that are completely cut by crack, while the "*square*" sign denotes the enriched elements that contain the crack-tip.
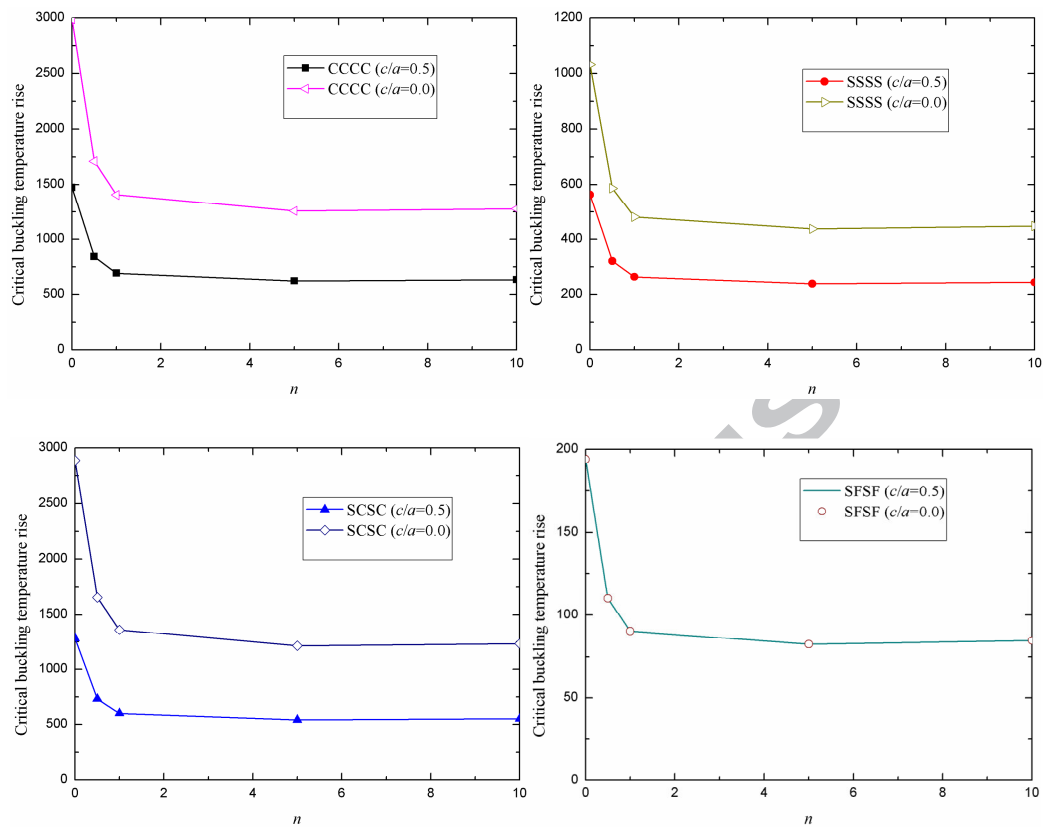
Fig. 4 Effect of crack and boundary conditions on the CBTR as a function of the volume fraction exponent of a rectangular Al/Al_2O_3 plate ($h/b = 0.1$).

Table 3. The CBTR of a rectangular Al/Al_2O_3 plate with an edge crack for different boundary conditions ($h/b = 0.01$, $c/a = 0.5$) altered by the volume fraction exponent.

n	CCCC	SCSC	SSSS	SFSF
0	17.036	14.415	6.225	1.960
0.5	9.665	8.176	3.531	1.111
1	7.930	6.707	2.897	0.911
5	7.236	6.123	2.644	0.833

Next, the study on the variation of the CBTR affected by the crack size is now explored. Similar to the previous example, we adopt different boundary conditions. We also employ a regular physical mesh of 31×15 elements for the analysis. Fig.5 shows the present numerical results of the CBTR as a function of crack sizes of an Al/Al$_2$O$_3$ plate with an edge crack with $n=1$ for various boundary conditions. It is evident that increasing the crack size leads to a decrease of the CBTR, which is found clearly for the cases of CCCC and SSSS and SCSC boundary conditions, while the CBTR for the SFSF varies very slightly, or it can be said, the variation of the CBTR with respect to the crack sizes. In other words, the crack sizes have no impact on the CBTR for the SFSF plate. In view of this phenomenon, when the crack size is set to be larger, the number of free boundaries of the plate is thus increased. In other words, the plates are more flexible now. The thermal forces in this circumstance can make the elastic energy in the system increases and as a result of decreasing the CBTR. Additionally, we again find that the CBTR of a fully clamped plate is much larger than that of simply supported one. Less constrains of plate from fully clamped to free or supported makes it freer and the elastic energy in the system is increased, which induces the decrease of the CBTR.
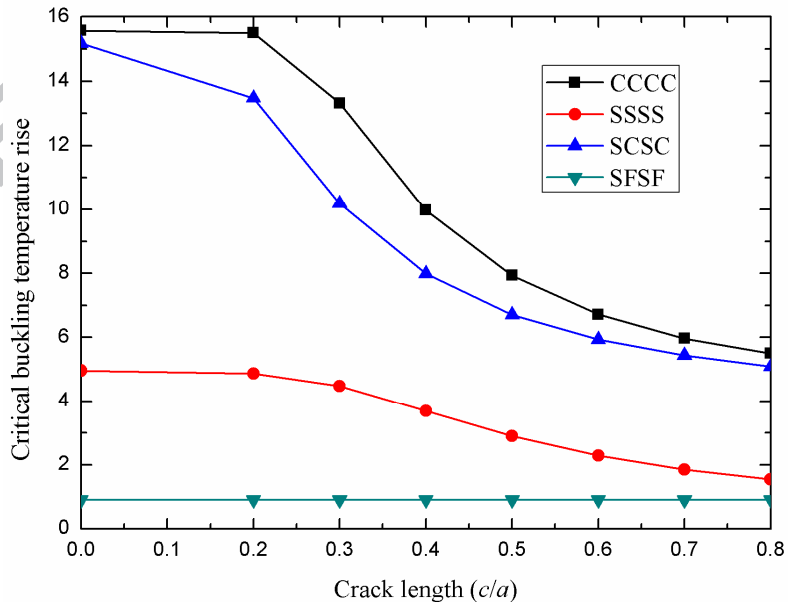

Fig. 5 Effect of crack size on the CBTR of a rectangular Al/Al$_2$O$_3$ plate with an edge

crack ($h/b = 0.01$) altered by the boundary conditions.

4.3. A square Al/ZrO₂ plate with an inclined central crack

A square Al/ZrO₂ plate with an inclined central crack subjected to a temperature rise as depicted in Fig. 6 is further studied. The length and thickness of plate are set to be a =1m, and h = 0.01m for this analysis.
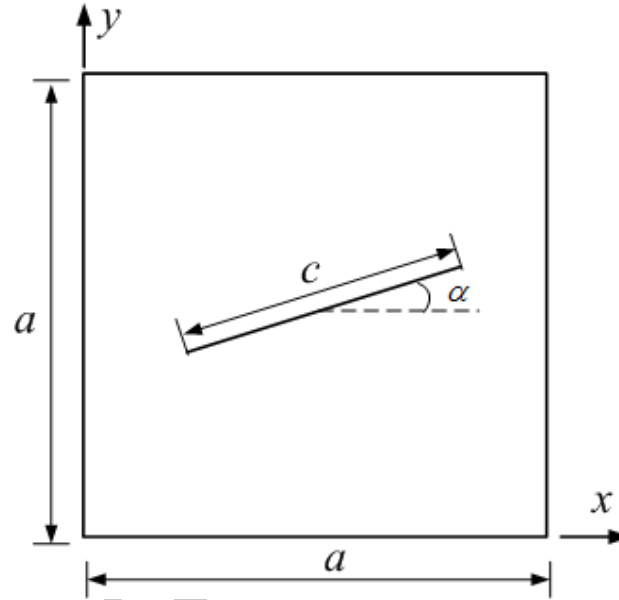

Fig. 6 The model geometry of a square Al/ZrO₂ with an inclined central crack.

This model of plate allows us to study the influence of the inclination of cracked angle α on the CBTR. We thus explore the effects of both the gradient index n and the inclination of cracked angle α on the CBTR. A regular physical mesh of 31×31 elements is used. Table 4 presents the gained numerical results of the CBTR of a fully simple supported Al/ZrO₂ plate account for different crack orientations varying from 0° to 90°. The present numerical results of the CBTR reveal that increasing the volume fraction exponent n induces a small decrease of the critical buckling load. The CBTR behaves symmetrically with respect to a crack orientation $\alpha = 45^o$ and it decreases as the crack orientation α increases. The same conclusion was drawn by Natarajan et al. [15], in which the XFEM was used. Consequently, the volume fraction exponent greatly alters the

critical thermal buckling temperature of FGPs.

Table 4

Effect of the inclined angle of crack on the CBTR of a fully simple supported Al/ZrO_2 plate (c/a =0.6) altered by volume fraction exponent.

n	Inclined angle (degree)						
	0	15	30	50	60	75	90
0	8.894	8.797	8.608	8.506	8.608	8.797	8.894
0.5	6.114	6.047	5.918	5.848	5.918	6.047	6.114
1	5.412	5.353	5.238	5.176	5.238	5.353	5.412
2	5.012	4.958	4.851	4.794	4.851	4.958	5.012
5	4.771	4.718	4.616	4.561	4.616	4.718	4.771

The effects of crack size and the boundary conditions on the CBTR are also studied for this square FGP. Fig.7 sketches the present results computed for the CBTR of a square Al/ZrO_2 plate with n =1 for different crack sizes and different boundary conditions. Similar to the previous example, it is again found here in the numerical results that the CBTR decreases with increasing the crack sizes, but this behavior can only be found for the plates with the CCCC and SSSS and SCSC boundary conditions. In the contrary, the present numerical results accounted for SFSF plate exhibit no any effects of the crack size on the CBTR. In other words, it can be concluded that not all the boundary conditions have impacts on the CBTR of FGPs, they possess different behaviors from each boundary condition to another boundary condition as clearly observed in the given numerical results.
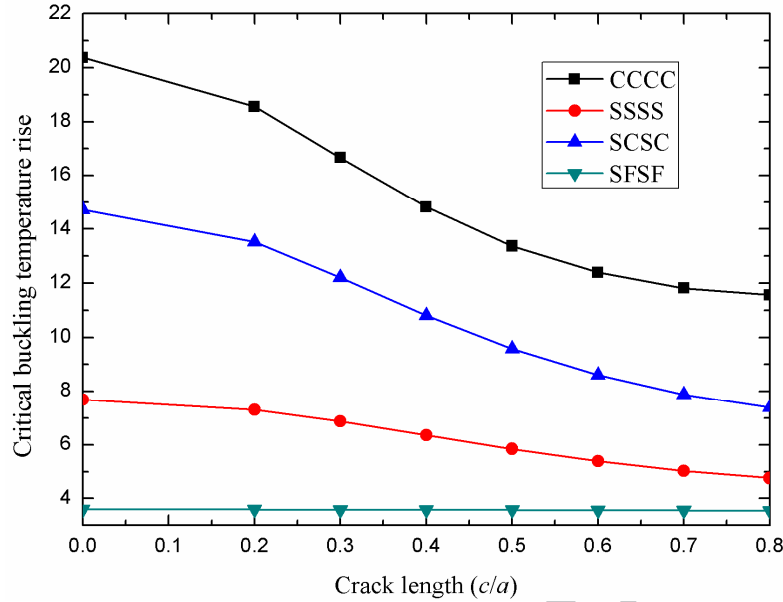
Fig. 7 Effect of crack size and boundary condition on the CBTR of a square Al/ZrO$_2$ plate for different boundary conditions.

4.4. A skewed FGP with an edge crack

Since the specific structures like skew plates have been applied to a variety of engineering application including, especially in the construction of aerospace, railway, civil and automotive structures. We thus devoted to the next numerical example by considering a skewed Al/Al$_2$O$_3$ plate with a = 2m, b=1m as schematically shown in Fig. 8. The aspect ratios such as h/b = 0.01 and c/a = 0.3 are taken for the analysis. In this study we adopt a regular physical mesh of 31×15 elements. We focus our attention on the numerical investigation of the effects of different gradient indexes, skew angles and the boundary conditions on the CBTR.
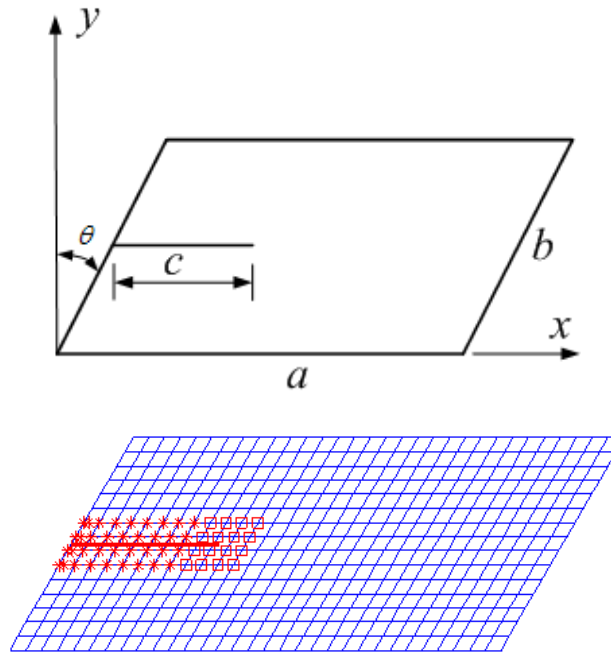
Fig. 8 Model geometry of a skewed plate with an edge crack and its regular physical mesh of a skew angle of $\theta = 30^{\circ}$ of 31×15 elements. The "*star*" sign represents the enriched elements that are completely cut by crack, while the "*square*" sign denotes the enriched elements that contain the crack-tip.

The effects of the gradient index and the boundary conditions on the CBTR are explored. Table 5 presents the computed numerical results of the CBTR of a skewed Al/Al$_2$O$_3$ plate with $\theta = 60^{\circ}$ for different volume fraction exponents and various boundary conditions including CCCC, SSSS, SCSC and SFSF. Not surprisingly, the behavior of the CBTR reported in Table 5 for this skew plate is quite similar to that accounted for the previous edge cracked rectangular FGP. It means that the gradient index *n* increases from 0 to 5 to five leads to a decrease of the CBTR for all the considered boundary conditions. Obviously, the plates with a fully clamped boundary condition yield a larger CBTR than that of a simply supported boundary condition.

Table 5

Effect of the volume fraction exponent and boundary conditions on the CBTR of a skewed

Al/Al$_2$O$_3$ plate with an edge crack ($\theta = 60^{\mathbf{o}}$).

n	CCCC	SCSC	SSSS	SFSF
0	3.451	3.451	0.622	0.578
0.5	1.956	1.956	0.355	0.331
1	1.604	1.604	0.2917	0.273
5	1.466	1.466	0.264	0.245
10	1.506	1.506	0.269	0.249

Figs.9 and 10 respectively presents the present numerical results of the CBTR computed by the developed XIGA for both fully clamped and simply supported skewed FGPs, taking into account the effect of the skew angles. We specifically take some skew angles of 15^0, 30^0, 45^0, 60^0, and 75^0. It is apparent that the influence of the skew angles on the CBTR is significant as the CBTR increases with increasing the skew angles. This physical behavior is found the same for two considered boundary conditions. Nevertheless, the values of the CBTR obtained by the clamped skewed FGPs are greater than those of the simply supported skewed FGPs.
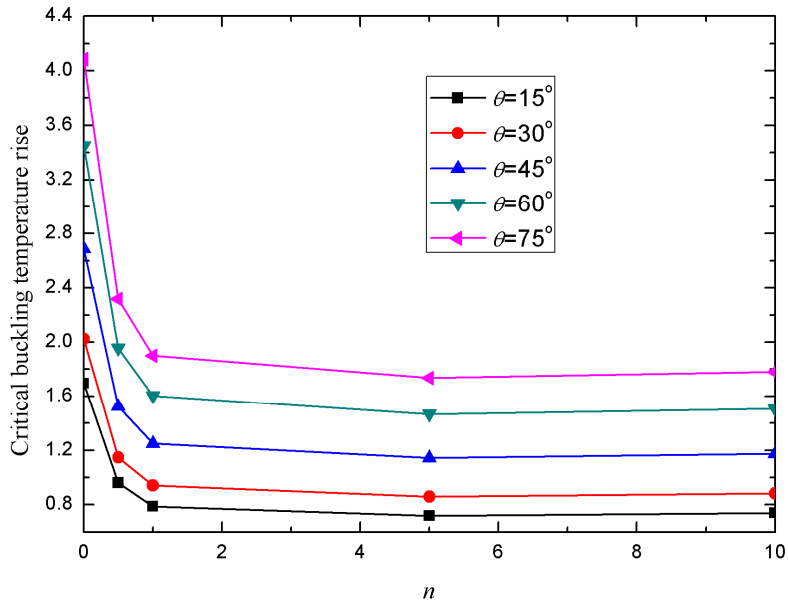
Fig. 9 Critical buckling temperature rise for a CCCC skewed FGP with different skew angles.
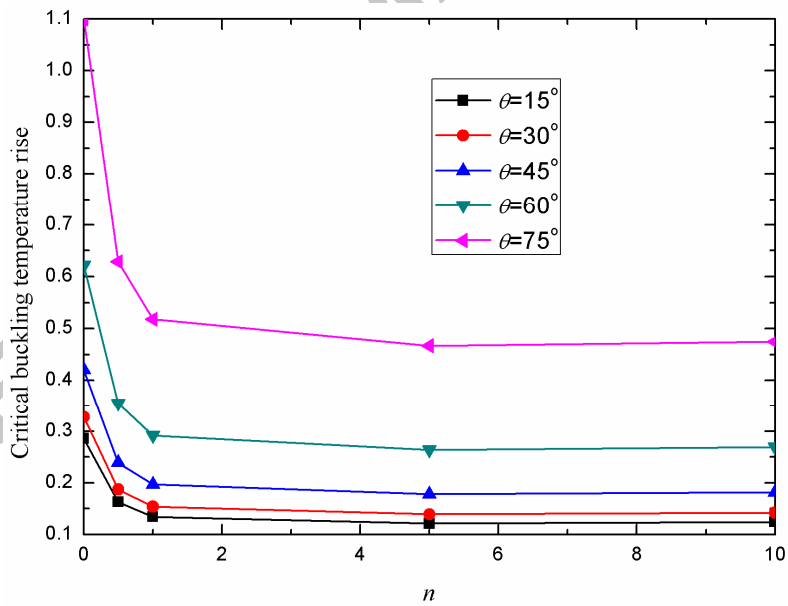

Fig. 10 Critical buckling temperature rise for a SSSS skewed FGP with different skew angles.

4.5. An Al/ZrO₂ plate with a cutout

The last example deals with a square Al/ZrO$_2$ plate with a circular cutout at the centre as schematically depicted in Fig. 11. The geometry parameters are: a=10m, a/h = 100, the radius r/a =0.1, and the boundary of the circular cutout is free of loading. Table 6 tabulates the convergence of the CBTR with respect to mesh size. Based on our own numerical experiments, it is indicated in the examination of the progressive refinements that a set of 18×18 elements is found to be adequate to model the full plate for the present analysis.
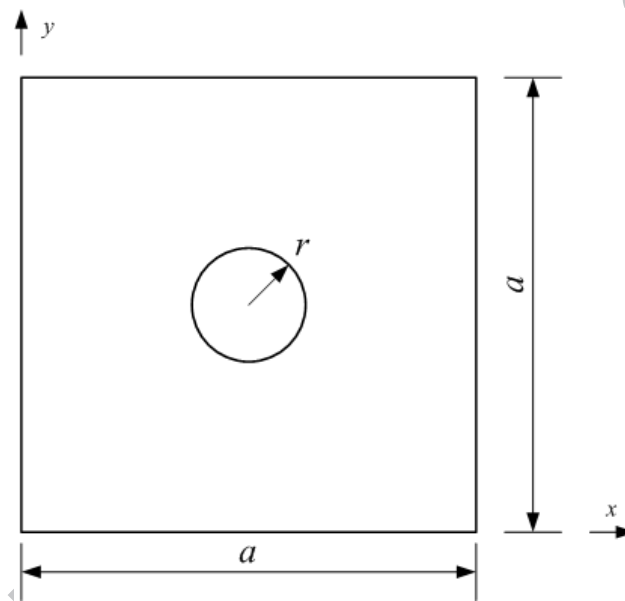

Fig. 11 Model geometry of a square plate with a circular cutout

Table 6

Convergence study of the CBTR for a simply supported square Al/ZrO$_2$ plate with circular cutout at the centre for accounted for different volume fraction exponents.

Elements	n		
	0	1	5
6×6	11.737	7.140	6.297
12×12	10.630	6.468	5.702
18×18	10.283	6.255	5.519
24×24	10.272	6.248	5.513

The influence of the aspect ratio of the radius $2r/a$, the gradient index n and the boundary conditions on the buckling behavior of an Al/ZrO$_2$ plate is numerically studied. Fig. 12 shows that increasing the radius $2r/a$ and gradient index n induces a decrease of the CBTR. The present numerical results are very interesting as they reveal also that the increase in the stiffness can cause an increase in the CBTR. It is important to observe from Fig.13 that the boundary conditions of FGPs in terms of the buckling analysis also alter the CBTR rise significantly. As expected, the CCCC plates yield a greater value of the CBTR compared with a SSSS one.

Furthermore, we add in this example the first four mode shapes of FGPs obtained by the XIGA. We account for different boundary conditions of SSSS, CCCC, CSCS and CFCF, and a radius of $2r/a$ =0.2 and a gradient index of n =0.5 are taken. The first four modes of buckling behavior are then shown in Fig. 14. Similar to the numerical results, the mode shapes vary significantly dependent upon the boundary conditions on which the plates are constrained.
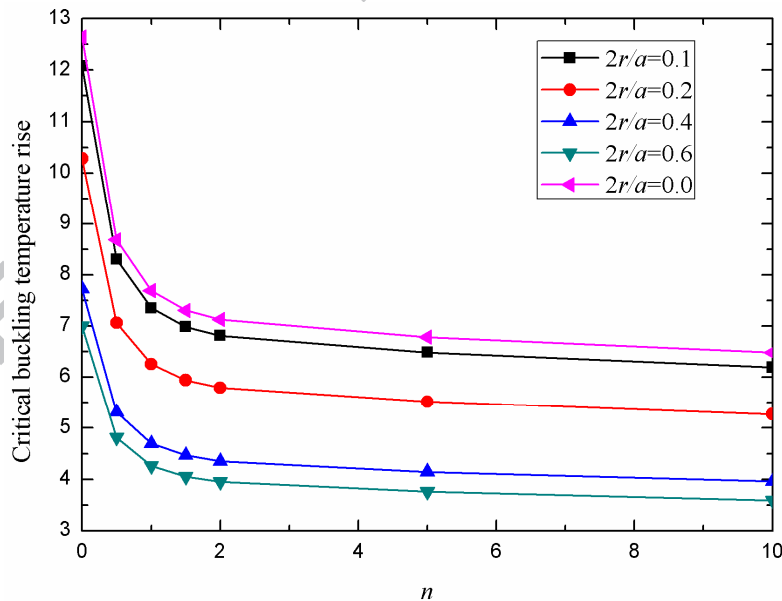

Fig. 12 Effect of the aspect ratio of radius to length ($2r/a$) and the volume fraction exponent on the CBTR for a SSSS square Al/ZrO$_2$ FGP.
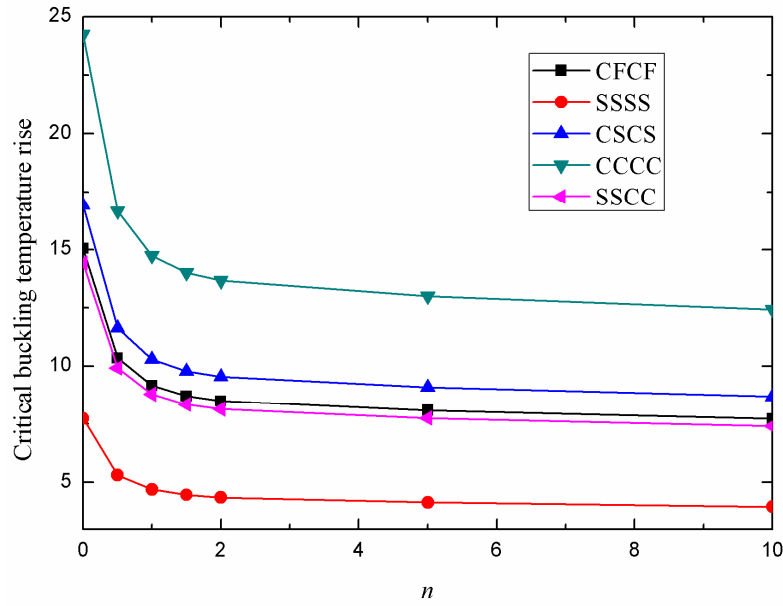
Fig. 13 Effect of the boundary conditions on the CBTR for a SSSS square Al/ZrO$_2$ FGP (2r/a =0.4) altered by the volume fraction exponent.

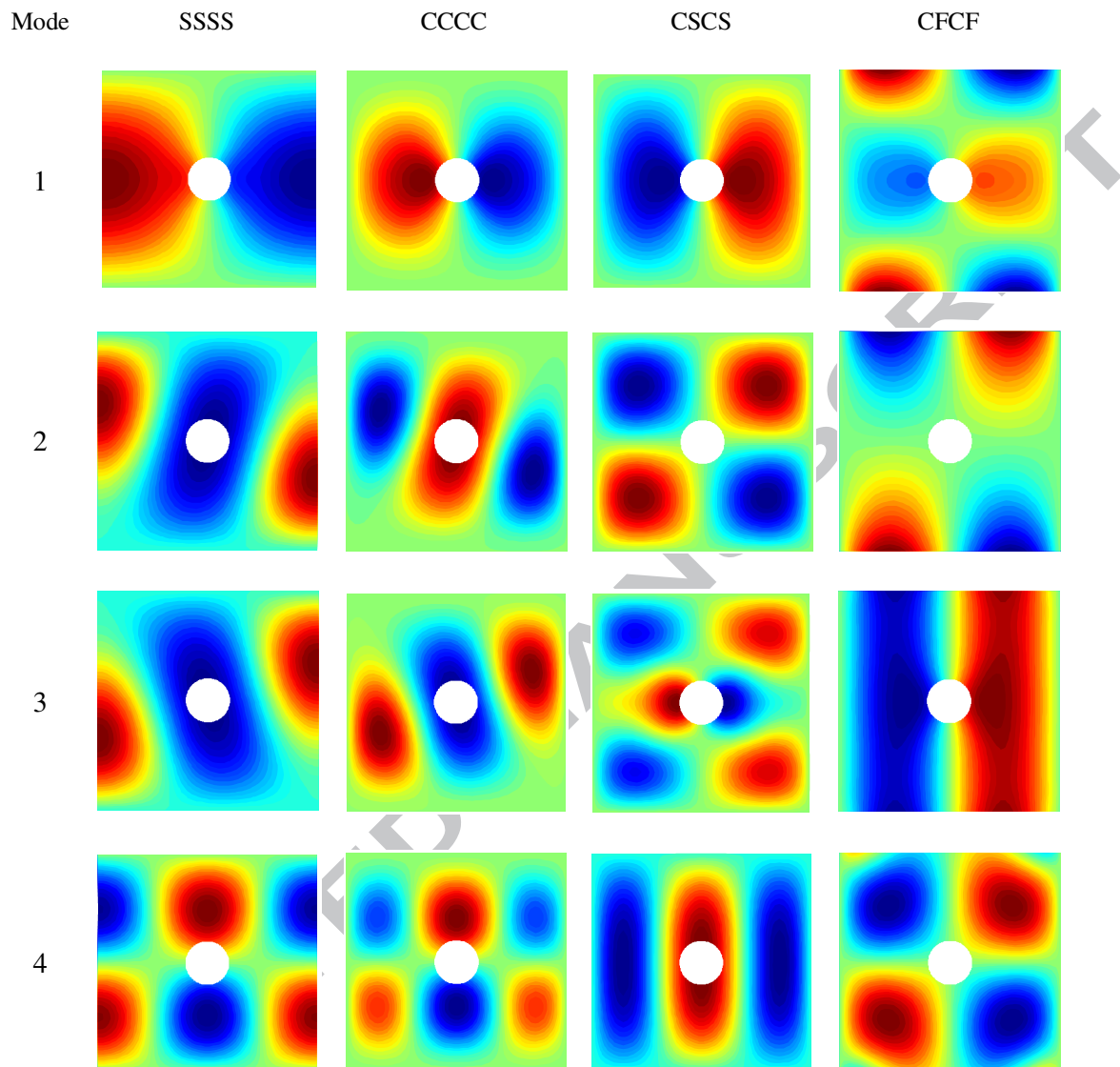| Mode	SSSS	CCCC	CSCS	CFCF

Fig. 14 The first four buckling mode shapes of a square Al/ZrO$_2$ FGP with a radius of 2r/a =0.2 and a gradient index n =0.5 for different boundary conditions.

The effect of cutout location on the CBTR of FGPs is additionally examined. A physical mesh of 24×24 is used, while the simply supported boundary condition is considered. We typically consider three center coordinates of the cutout, e.g., (2m, 8m), (5m, 8m), and (8m, 8m) for a radius of $2r/a$ =0.2. The numerical results of the CBTR for a simply supported FGM plate are reported in Table 7. For this particular case of study, the present numerical results reveal an insignificant effect of the location of the cutout on the CBTR. Numerically, we find that the CBTR for the plate with the cutout located at the center is slight smaller than that for the other cases. Loosely speaking, it might be understood that the plates become highly critical if the defects or cutout locate closer to their boundaries, where the tendency of damaging the structures becomes highly possible.

Also in Table 7, interestingly, the volume fraction exponent greatly alters the CBTR with different locations of the cutout. The CBTR decreases with increasing the volume fraction. Furthermore, the first four buckling mode shapes of FGPs obtained by the XIGA for different cutout locations with a radius of $2r/a$ =0.2 and a gradient index n =1 are also depicted in Fig. 15. Clearly, the same boundary conditions and the same plates, but the buckling modes vary dependently on the location of the cutout.

Table 7

The CBTR for a simply supported square Al/ZrO$_2$ plate with a circular cutout considering different locations and various volume fraction exponents.

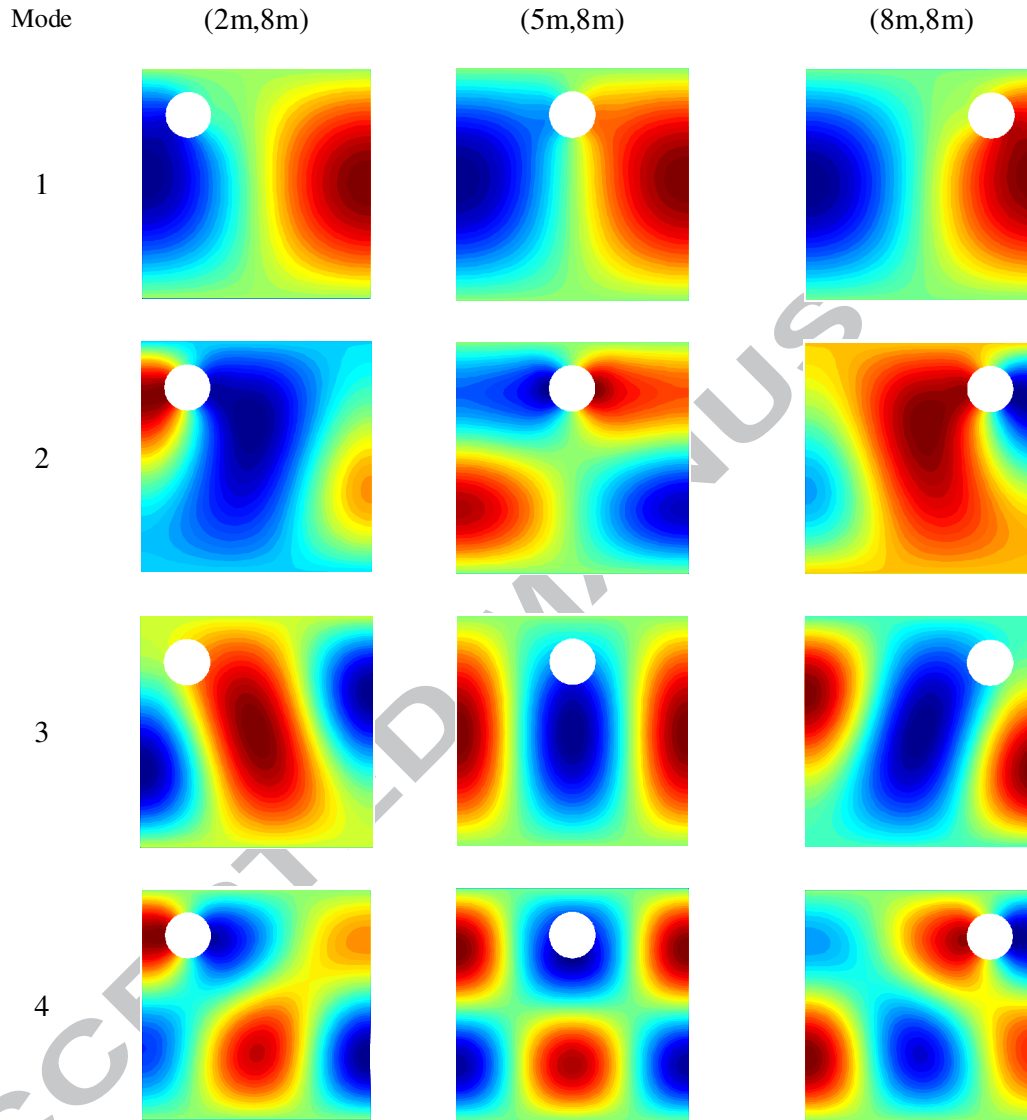| Center coordinates	n		
of the cutout	0	1	5
(2m,8m)	12.347	7.510	6.627
(5m,8m)	12.043	7.324	6.463
(8m,8m)	12.347	7.510	6.627
(5m,5m)	10.272	6.248	5.513

Fig. 15 The first four mode shapes of a SSSS square Al/ZrO$_2$ FGP with the radius $2r/a$ =0.2 and the gradient index n =1 for different cutout locations.

5. Conclusions

We develop an effective and accurate NURBS-based XIGA using the first-order shear deformation plate theory for the analysis of thermal buckling behaviors of FGPs with

internal defects such as cracks or cutouts. In this formulation, the trimmed NURBS surface to describe the geometrical structure with cutouts is no longer required as the internal discontinuity is independent of the mesh, as a result of utilizing the level sets. The accuracy of the CBTR obtained by the developed XIGA is high and in good agreements with the reference solutions for both thin and moderately thick plates with internal defects. The influences of gradient index, crack location, crack length, width to thickness, cutout size, and boundary conditions on the CBTR are investigated. Some major conclusions drawn from the study can be summarized as follows:

- Upon investigations carried out according to the numerical results presented, the developed approach based on XIGA using NURBS associated with the FSDT is shown to be ideal candidates for estimating the thermal buckling coefficients of FGPs, exhibiting a good agreement between the obtained results with the reference solutions.

- The effects of the boundary conditions and the volume fraction exponents on the CBTR of FGPs are significant. The clamped FGPs yield a greater CBTR than the simply supported FGPs.

- The behavior of the CBTR of square plates with an inclined central crack is found to be symmetric with respect to a crack orientation $\alpha = 45^{\circ}$ and it decreases as the crack orientation α increases.

- The skew angle has a critical impact on the CBTR. Increasing the skew angles lead to to an increase of the CBTR. The CBTR of clamped skewed FGPs are larger than those of simply supported skewed FGPs.

- Increasing the cutout size and gradient index n leads to a decrease of the CBTR of FGPs. Again, the boundary conditions significantly alter the CBTR of FGPs with internal cutout. Additionally, the location of the cutout also owns an important influence on the CBTR. The cutout or defect locates closer to the boundary of the plate induces a greater CBTR than the cutout locates at the center.

- Knowledge that has drawn from the study may be helpful to the design and development of the FGMs and FGP structures in advanced engineering

applications.

- Nevertheless, the present formulation is potential and has no limitation. As a result, definitely, its further extension to other problems is promising.

References

[1] Jha DK, Kant T, Singh RK. A critical review of recent research on functionally graded plates. Compos Struct 2013;96:833-49.

[2] Fantuzzi N, Tornabene F, Viola E. Four-parameter functionally graded cracked plates of arbitrary shape: A GDQFEM solution for free vibrations. Mechanics of Advanced Materials and Structures 2016;23(1):89-107.

[3] Huang CS, McGee III OG, Chang MJ. Vibrations of cracked rectangular FGM thick plates. Composite Structures 2011;93(7):1747-1764.

[4] Javaheri R, Eslami MR. Thermal buckling of functionally graded plates. AIAA J 2002;40(1):162-9.

[5] Shariat BAS, Eslami MR. Buckling of thick functionally graded plates under mechanical and thermal loads. Compos Struct 2007;78(3):433-9.

[6] Woo J, Meguid SA. Thermomechanical postbuckling analysis of functionally graded plates and shallow cylindrical shells. Acta Mechanica 2003;165(1-2):99-115 .

[7] Najafizadeh MM, Heydari HR. Thermal buckling of functionally graded circular plates based on higher order shear deformation plate theory. Eur J Mech-A/Solids 2004;23(6):1085-100.

[8] Khalfi Y, Hourai MSA, Tounsi A. A refined and simple shear deformation theory for thermal buckling of solar functionally graded plates on elastic foundation. Int J Comput. Methods 2014;11(5): 1350071,20P.

[9] Malekzadeh P. Three-dimensional thermal buckling analysis of functionally graded arbitrary straight-sided quadrilateral plates using differential quadrature method. Compos Struct 2011;93(4):1246-54.

[10] Samsam Shariat BA, Eslami MR. Thermal buckling of imperfect functionally graded plates. Int J Solids Struct 2006;43(14-15):4082-96.

[11] Jaberzadeh E, Azhari M, Boroomand B. Thermal buckling of functionally graded skew and trapezoidal plates with different boundary conditions using the element-free Galerkin method. Eur J Mech-A/Solids 2013;42:18-26.

[12] Zhao X, Lee YY, Liew KM. Mechanical and thermal buckling analysis of functionally graded plates. Compos Struct 2009;90(2):161-71.

[13] Saji D, Varughese B, Pradhan SC. Finite element analysis for thermal buckling behaviour in functionally graded plates with cut-outs. Proceedings of the International Conferenceon Aerospace Science and Technology, Bangalore, India, 2008.

[14] Shaterzadeh A, Abolghasemi S, Rezaei R. Finite element analysis of thermal buckling of rectangular laminated composite plates with circular cutout. J Therm Stresses 2014;37(5):604-23.

[15] Natarajan S, Chakraborty S, Ganapathi M, Subramanian M. A parametric study on the buckling of functionally graded material plates with internal discontinuities using the partition of unity method. Eur J Mech –A/Solids 2014;44:136-47.

[16] Hughes TJR, Cottrell JA, Bazilevs Y. Isogeometric analysis: CAD, finite elements, NURBS, exact geometry and mesh refinement. Comput Methods Appl Mech Eng 2005;194(39-41):4135-95.

[17] Valizadeh N, Natarajan S, Gonzalez-Estrada OA, Rabczuk T, Bui TQ, Bordas SPA. NURBS-based finite element analysis of functionally graded plates: static bending, vibration, buckling and flutter. Compos Struct 2013;99:309-26.

[18] Yu TT, Yin SH, Bui QT, Hirose S. A simple FSDT-based isogeometric analysis for geometrically nonlinear analysis of functionally graded plates. Finite Elemt. Anal. Des.

2015; 96:1-10.

[19] Yin SH, Hale JS, Yu TT, Bui TQ, Bordas SPA. Isogeometric locking-free plate element: A simple first order shear deformation theory for functionally graded plates. Compos Struct 2014;118:121-38.

[20] Bui QT. Extended isogeometric dynamic and static fracture analysis for cracks in piezoelectric materials using NURBS. Comput Methods Appl Mech Eng 2015; 295:470-509.

[21] Bazilevs Y, Calo VM, Hughes TJR, Zhang Y. Isogeometric fluid–structure interaction: theory, algorithms, and computations. Comput Mech 2008;43(1);3-37.

[22] Lu J. Isogeometric contact analysis: Geometric basis and formulation for frictionless contact. Comput Methods Appl Mech Eng 2011;200(5-8):726-41.

[23] Nguyen MN, Bui QT, Yu TT, Hirose S. Isogeometric analysis for unsaturated flow problems. Computers and Geotechnics 2014;62:257-67.

[24] Yin SH, Yu TT, Bui QT, Nguyen NM. Geometrically nonlinear analysis of functionally graded plates using isogeometric analysis. Eng. Comput. 2015; 32:519-558.

[25] Ghorashi SS, Valizadeh N, Mohammadi S. Extended isogeometric analysis for simulation of stationary and propagating cracks. Int J Numer Methods Eng 2012;89(9):1069-101.

[26]De Luycker E, Benson DJ, Belytschko T, Bazilevs Y, Hsu MC. X-FEM in isogeometric analysis for linear fracture mechanics. Int J Numer Meth Eng. 2011; 87(6):541-65.

[27] Benson DJ, Bazilevs Y, De Luycker E, Hsu MC, Scott M, Hughes TJR, Belytschko T. A generalized finite element formulation for arbitrary basis functions: From isogeometric analysis to XFEM. Int J Numer Meth Eng. 2010;83(6):765-85.

[28] Yu TT, Lai YL, Yin SH. Dynamic crack analysis in isotropic/orthotropic media via extended isogeometric analysis. Mathematical Problems in Engineering 2014. Article ID 725795, 11p.

[29] Haasemann G, Kästner M, Prüger S, Ulbricht V. Development of a quadratic finite element formulation based on the XFEM and NURBS. Int J Numer Methods Engng 2011; 86(4-5):598-617.

[30]Tran Loc V, Ly HA, Lee JH, Abdel Wahab M, Nguyen-Xuan H. Vibration analysis of cracked FGM plates using higher-order shear deformation theory and extended isogeometric approach. International Journal of Mechanical Sciences 2015;96-97:65-78.

[31]Bhardwaj G, Singh IV, Mishra BK. Stochastic fatigue crack growth simulation of interfacial crack in bi-layered FGMs using XIGA. Computer Methods in Applied Mechanics and Engineering 2015;284:186-229.

[32] Piegl LA, Tiller W. The NURBS book. Berlin: Springer;1996.

[33] Thai CH, Nguyen-Xuan H, Nguyen-Thanh N, Le TH, Nguyen-Thoi T, Rabczuk T. Static, free vibration and buckling analysis of laminated composite Reissner–Mindlin plates using NURBS based isogeometric approach. Int J Numer Methods Eng 2012;91(6):571-603.

[34] Liu P, Bui QT, Zhu D, Yu TT, Wang JW, Yin SH, Hirose S. Buckling failure analysis of cracked functionally graded plates by a stabilized discrete shear gap extended 3-node triangular plate element. Composites Part B: Eng. 2015; 77:179-193.

[35] Yu TT, Bui QT, Liu P, Hirose S. A stabilized discrete shear gap extended finite element for the analysis of cracked Reissner-Mindlin plate vibration problems involving distorted meshes. Int J Mech Mater Des 2015 (in press) http://dx.doi.org/10.1007/s40430-014-0232-1

[36] Bhardwaj G, Singh IV, Mishra BK, Bui QT. Numerical simulation of functionally graded cracked plates using NURBS based XIGA under different loads and boundary conditions. Compos. Struct. 2015; 126:347-359.

[37] Sukumar N, Chopp DL, Moës N, Belytschko T. Modeling holes and inclusions by level sets in the extended finite element method. Comput Methods Appl Mech Eng 2001;190(46-47):6183-200.

[38] Yin SH, Yu TT, Bui QT, Xia SF, Hirose S. A cutout isogeometric analysis for thin laminated composite plates using level sets. Compos. Struct. 2015;127:152-164.

[39] Wu LH. Thermal buckling of a simply supported moderately thick rectangular FGM plate. Compos. Struct. 2004;64(2):211-218.